Journal Pre-proof

1000 K optical ratiometric thermometer based on Er^{3+} luminescence in yttrium gallium garnet

M.A. Hernández-Rodríguez, K. Kamada, A. Yoshikawa, J.E. Muñoz-Santiuste, A. Casasnovas-Melián, I.R. Martín, U.R. Rodríguez-Mendoza, V. Lavín

This is a PDF file of an article that has undergone enhancements after acceptance, such as the addition of a cover page and metadata, and formatting for readability, but it is not yet the definitive version of record. This version will undergo additional copyediting, typesetting and review before it is published in its final form, but we are providing this version to give early visibility of the article. Please note that, during the production process, errors may be discovered which could affect the content, and all legal disclaimers that apply to the journal pertain.

1000 K optical ratiometric thermometer based on Er³⁺ luminescence in yttrium gallium garnet

M.A. Hernández-Rodríguez,[a,*] K. Kamada,[b,c] A. Yoshikawa,[b,c,d] J.E. Muñoz-Santiuste,[e]
A. Casasnovas-Melián,[f] I.R. Martín,[f] U.R. Rodríguez-Mendoza,[f] V. Lavín[f]

[a] Phantom-G, CICECO – Aveiro Institute of Materials. Department of Physics, Universidade de Aveiro, Aveiro 3810-193, Portugal
[b] New Industry Creation Hatchery Center (NICHe), Tohoku University, 6-6-10 Aoba, Aramaki, Sendai 980-8579, Japan.
[c] C&A Corporation, Sendai 980-8579, Japan.
[d] Institute for Materials Research, Tohoku University, 2-1-1 Katahira, Sendai 980-8577, Japan
[e] Departamento de Física, and MALTA Consolider Team, Escuela Politécnica Superior, Universidad Carlos III de Madrid, Avenida de la Universidad 30, E-28913 Leganés, Madrid, Spain
[f] Departamento de Física, MALTA Consolider Team, IMN, and IUdEA, Universidad de La Laguna, Apdo. Correos 456, E-38200 San Cristóbal de La Laguna, Santa Cruz de Tenerife, Spain

Abstract

The temperature dependence of the Er³⁺ green luminescence in $Y_3Ga_5O_{12}$ crystal were analysed under ultraviolet and near-infrared laser excitations for optical sensing purposes. Changes in the relative green emission intensities from the $^2H_{11/2}$ and $^4S_{3/2}$ thermally-coupled multiplets to the $^4I_{15/2}$ ground state were measured from room temperature up to 1000 K. The calibrated temperature scale shows a maximum in the absolute thermal sensitivity of ~23.9 x 10^{-4} K^{-1} at 580 K and a relative thermal sensitivity of ~1.36 % K^{-1} at RT, combining results for both blue and near-infrared laser excitations. The excellent results obtained, compared with other Er³⁺-based optical temperature sensors, are a consequence of the advantages of garnet crystals as optically efficient hosts that, apart from an impressive capability to be synthesized both as bulk and fiber forms, allow extending the long working temperature range up to 1000 K, and beyond, to the melting point limit close to 2000 K. In addition, the use of green emissions for the temperature calibration, with negligible black-body radiation disturbance, only needs a low-cost, basic setup that uses commercially available lenses, lasers and detectors. All these facts support the Er³⁺-doped $Y_3Ga_5O_{12}$ garnet crystal as a potential candidate as temperature sensor, showing large sensitivity and good temperature resolution for ultra-high temperature industrial applications.

Corresponding author *: M.A. Hernández-Rodríguez (miguelandreshr@ua.pt)

1. Introduction

Temperature (T) is the most widely measured variable in industrial equipment and processing, in which damage prevention is the key word. The importance of controlling and/or measuring temperature in many daily life devices and in modern technology can be quantified: T-sensor market size overcame 7 billion USD in 2019 and is estimated to increase ~4% (compound annual growth rate) between 2020 and 2026 [1,2]. This growth is being boosted by new applications, such as healthcare equipment, home smart sensing, industrial automatization, food safety, and space sensing. Thermal accuracy and performance of industrial equipment, analytical instrumentations, and medical devices are relevant parameters to take into account when selecting the best T-sensor, in which parameters such as operating environment and range, location, material compatibility and sensitivity variables, among others, must be evaluated throughout the design process [3].

In this global market, the four most sold T-sensors, ranging in responsiveness and accuracy from high to low, are negative coefficient thermistors (up to 425 K), resistance temperature detectors (up to 900 K), thermocouples (up to 2000 K) and semiconductors-based sensors (up to 425 K) [4]. However, nowadays specialized industrial processes at extreme conditions, i.e. low or high temperatures and/or pressure, inert or acid environments, etc, in micro- and nano-sized devices are gaining relevance [5]. Thus there is an increasingly demand to design temperature [6–15], pressure [14–18] and/or pH sensors capable to calibrate and control such processes. Focusing on the optical temperature sensors (OTS) field, research has been greatly stimulated by the requirement for remote, non-contact, safe, inexpensive, and reliable sensors in monitoring body temperature, e.g., as a fast testing of COVID-19 effects, and the electrical transformer temperature in sensitive industrial environments, especially those related to oil refinery industry. OTS are also especially useful in biomedicine and nanoengineering fields, in which spatially-resolved temperature control of hot spots in hardware architecture or a deeper skin penetration depth of temperature readouts are necessary [19]. The known benefits of OTS, compared to traditional electronic sensors, include insensitivity to electromagnetic interference, large stability to environment, and possibility of remote sensing. Well known Bragg grating and Fabry-Perot cavity architectures applied on metal-coated fused silica and sapphire fibers have proven to be useful as OTS up to around 1300 and 1800 K, respectively, although high temperature stability is still under testing [20–23]. Others commonly OTS, used in the nanoscale, are carbon nanostructures, quantum dots, porous silicon, organic particles and lanthanide-doped nanocrystals [24].

Two basic elements are required in OTS: an optically active material, in the form of bulk, fiber or nanoparticle that will be placed physically at the desired position, and an optical setup, which basically consists of an excitation laser source and a detection system [25,26]. The main advantage of these sensors resides in the absence of physical wire connecting different components, since the propagation of the electromagnetic fields in the optical range does not require them. In OTS, the readout of temperature comes from changes in the photoluminescence of the optically active material that can be manifested in many ways, such as the relative intensities of thermally-coupled emissions, the lifetime of the excited states, the polarization of the emission, the line-shape of the bands, the energy-shift of the bands, etc. [19]. Many OTS uses the luminescence intensity ratio (LIR) method, which is the most widely used technique to calibrate temperature. This technique relies on calibrating the dependence of temperature of the active material on the relative intensities of two thermally-coupled emissions [25,26]. The main advantages of the LIR technique for temperature sensing are its insensitivity to fluctuations of the laser excitation source and to noise in the detection system. In addition, for low pumping power, i.e., in a "quasi-thermal equilibrium", the intensity ratio does not depend on the laser source but on the populations of the involved levels and their de-excitation probabilities. Otherwise, laser power may increase the temperature of the sample, generating phonons in the optically active material and breaking the thermal equilibrium of the OTS.

Temperature sensing based on lanthanide (Ln^{3+}) ions luminescence in the optical (UV-Vis-NIR) range uses a pair of $^{2S+1}L_J$ multiplets whose energy gap is of the order of thermal energy. This assures the thermally-induced population of the upper multiplet at the expenses of the population of the lower one. Some of the trivalent lanthanides (Ln^{3+}) ions present this kind of thermally-coupled emitting multiplets useful for sensing purposes, such as Praseodimium (Pr^{3+}), Neodymium (Nd^{3+}), Europium (Eu^{3+}), Holmium (Ho^{3+}), Erbium (Er^{3+}) and Thulium (Tm^{3+}) [27]. In particular, trivalent Erbium (Er^{3+}) takes advantage of the thermally-coupled green emitting levels, which can be easily excited using low-cost violet, blue, green or NIR lasers, as well as the negligible system´s blackbody radiation overlapping effects at very high temperature.

Concerning host materials, Ln^{3+}-doped, glass-based OTS have been proven to operate up to ~750 K to the best, since they are limited to work below the glass transition temperature [28–33]. Although this limit is overtaken up to 1000 K by lanthanide-doped nanocrystals [34], bulk crystals with high melting temperature can be potential low-cost materials for sensing at even higher temperature in industrial applications. Garnet crystals, with an

impressive capability to be synthesized in a shape-controlled way in cylindrical, prismatic pixel array or fiber forms [35–40], and a melting temperature in the range of 2000-2300 K [41,42] seem to be ideal candidates for OTS at very high temperature in industrial applications. In addition, properties such as high mechanical strength and good thermal and optical properties have made the garnet family one of the most used host matrices for doping with Ln^{3+} optically active ions as laser medium [43] and scintillators, widely used in many detection systems addressing different fields, such as medical imaging, homeland security, industrial control, oil drilling exploration, and high energy physics calorimetry [35,37,39,44].

In this work, we present the temperature-dependent Stokes and upconverted emissions of Er^{3+} ions in $Y_3Ga_5O_{12}$ (YGG) garnet bulk crystal, synthesized by the micro-pulling technique and with the capability to be shape-controlled as cylindrical bulk, prismatic pixel array or fiber forms with high transparency, in order to analyse its viability as a versatile and large working range OTS for industrial applications up to, and beyond, 1000 K.

2. Experimental

The $Y_3Ga_5O_{12}$ single crystals doped with x=0.1 and 1 at.% Er^{3+} in the melt were synthesized by the micro-pulling down (μ-PD) growing technique using an iridium crucible under (Ar + 2% O_2) atmosphere with an RF heating system at the Institute for Materials Research (IMR, Tohoku University, Japan) [45]. For the synthesis, stoichiometric mixture of 4N Y_2O_3, β-Ga_2O_3 and Er_2O_3 powders (Iwatani Co.) was used as starting material. The μ-PD technique consists on a continuous transport of the melted material through holes at the bottom of the crucible and its continuous solidification in a liquid, or solid, interface [45–47]. The melt and the crystal are pulled down with different velocities [48]. The general procedure followed to grow crystals through this technique is composed of several stages. Firstly, the crucible is charged with a mixture of powders and then, it is heated until these materials are completely melted. After this, the seed is displaced upward until it reaches the crucible, forming the meniscus and partially melting the top of the seed. The shape of the meniscus is continuously corrected through adjusting the crucible temperature and the position of the seed crystal. The YGG crystal was grown using a seed of a <100> oriented $Y_3Al_5O_{12}$ crystal and a pulling rate of 0.05–0.07 mm/min. Finally, the grown crystal, with typical diameter of 3 mm and length of 20 mm, is separated from the meniscus and they are cooled to room temperature. The μ-PD growth apparatus for garnet crystals is shown elsewhere [35].

Optical properties of Ln^{3+} ions are ruled by their local structure in host matrix. The fine structure of $^{2S+1}L_J$ multiplets and the forced intra-configurational *4f-4f* electric-dipole

transition probabilities in the optical (UV-VIS-NIR) range are intimately related to this local environment. X-ray diffraction pattern (not shown) indicates that the yttrium garnet crystallizes in the *Ia-3d* cubic space group, in which Y^{3+} is surrounded by eight oxygen ligands with two main distances (2.36 and 2.46 Å) and Ga^{3+} ions occupy two inequivalent sites, i.e., a short GaO_4 tetrahedra with a bonding distance of 1.87 Å and a GaO_6 octahedra with a longer bonding distance of 2.02 Å [35]. The Er^{3+} ion replaces, without charge compensation, the yttrium one showing a distorted D_2 local point symmetry that leads to the total breakdown the $^{2S+1}L_J$ multiplets degeneracies to give (2J + 1)/2 crystal-field, or Stark, levels [49]. It is worth noting that the garnet structure is stable up to its melting point (2000-2300 K).

The absorption spectrum in the visible and NIR ranges was measured using a spectrophotometer (Varian Cary 5000). Temperature-dependent Stokes and upconverted photoluminescence experiments from room temperature (RT) up to 1053 K and 983 K, respectively, are described elsewhere [35]. For temporal dynamic measurements, a 10 ns pulsed optical parametric oscillator OPO (EKSPLA/NT342/3/UVE) was used, and the green luminescence was detected by a photomultiplier (Hamamatsu R928) through a single grating monochromator (Jobin-Yvon Triax 180) connected to a digital oscilloscope (LeCroy WS424). All spectra were corrected from the instrument response.

3. Luminescence intensity ratio technique

LIR technique has been used to calibrate a temperature scale up to, and beyond, 1000 K using an optically active material, i.e., Er^{3+}-doped YGG garnet crystal, exploiting the changes in the relative intensities of the green emissions from the $^2H_{11/2}$ and $^4S_{3/2}$ multiplets to the $^4I_{15/2}$ ground state with temperature. This temperature dependence can be easily understood using only three energy levels, i.e., the ground state E_0 ($^4I_{15/2}$ level), and the excited states E_1 ($^4S_{3/2}$ level) and E_2 ($^2H_{11/2}$ level) (see **Figure 1**). With the structural data of the Er^{3+} local environment in YGG, a crystal-field calculation was performed to obtain all the energy level information of this optically active ion in this garnet crystal [50]. The thermally coupled multiplets, located in the 18400 – 19400 cm^{-1} range (see **Figure 1**), show an energy gap of $E_{21} \sim 763$ cm^{-1} that is of the order of magnitude of the thermal energy $k_B T$ at RT (~ 200 cm^{-1}), allowing a sharing of population between both multiplets that, in thermal equilibrium, follows a Boltzmann distribution. The Er^{3+} ions in both multiplets de-excitate to the ground state and the energy involved in this transition is partially emitted as green photons with different probabilities, being larger for the $^2H_{11/2}$ multiplet, as it will be shown later from

5

Judd-Ofelt calculations [50]. In fact, the $^2H_{11/2}\rightarrow^4I_{15/2}$ transition is known to be hypersensitive [33,51], i.e., its intensity shows a high sensitivity to the sort of ligand environment (ligand type, coordination number, RE-ligand bond length, local site symmetry, covalency, etc…) constituting the Er^{3+} first coordination sphere [52].
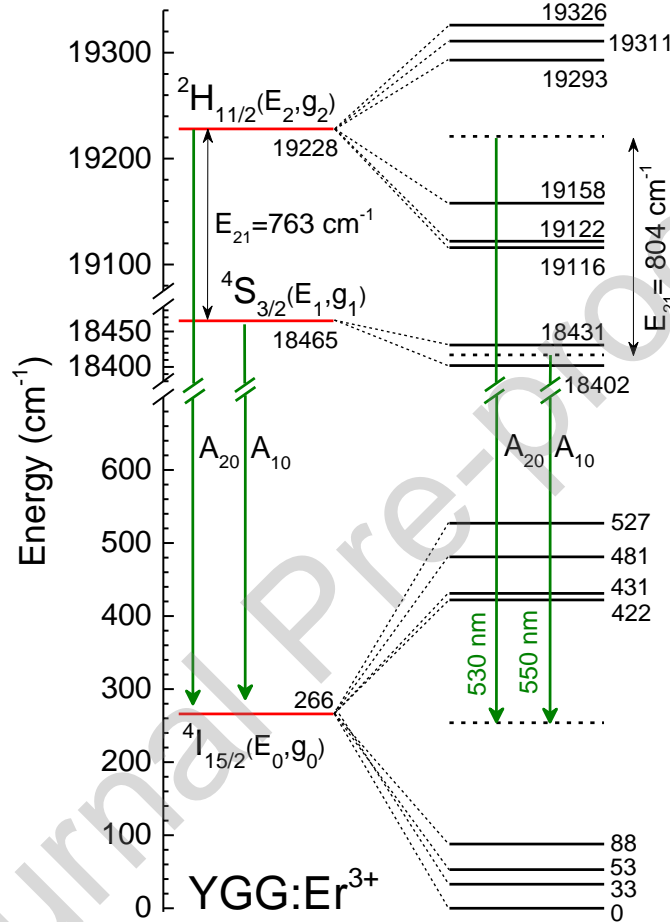

Figure 1. Energy level diagram of the three levels system involved in the thermalized green emissions of Er^{3+} ion in $Y_3Ga_5O_{12}$ garnet crystal, calculated using the crystal-field theory. Multiplets (in red) and Stark levels (in black) are given, together with the barycentre, or centres of gravity, of the Stark levels (dashed horizontal lines). E_{21} is the energy gap between the two excited thermalized levels; g_i is the degeneracy of the i-th level; and A_{ij} is the spontaneous photon emission rate between the i-th and j-th levels.

Thus the Boltzmann's distribution law describes the intensity behaviour of these thermalized multiplets as a function of temperature as follows [19,27,53,54]

$$LIR = \frac{I_{20}}{I_{10}} = \left(\frac{c_{20}A_{20}h\nu_2}{c_{10}A_{10}h\nu_1}\right)\cdot\left(\frac{N_2}{N_1}\right) = \left(\frac{c_{20}A_{20}h\nu_2}{c_{10}A_{10}h\nu_1}\right)\cdot\left(\frac{g_2}{g_1}\right)\cdot e^{-E_{21}/k_BT} = C\cdot e^{-E_{21}/k_BT} \qquad (1)$$

where I_{10} and I_{20} are the areas under the green emissions bands of thermalized multiplets, and N_1 and N_2 are the populations of the E_1 and E_2 multiplets, respectively, whose N_2/N_1 relative value follows the Boltzmann's distribution law, if the laser power does not heat the host

matrix. This relative population is ruled by the exponential factor, which includes the temperature T of the host matrix and the environment; the Boltzmann constant k_B; and the energy gap E_{21} between the pair of thermalized multiplets. On the other hand, the pre-exponential factor C depends on different parameters: the instrument response c_{i0}, which is equal to unity since emission spectra have been corrected from the setup response; the energy of the transition from each multiplet to the ground state $h\nu_i$; the degeneracies of the multiplets g_i; and the spontaneous emission rates A_{20} and A_{10} of the E_2 and E_1 multiplets to the E_0 ground state, respectively. These rates can be written as $A_{20} = \beta_{20} \cdot A_2$ and $A_{10} = \beta_{10} \cdot A_1$, being β_{i0} the branching ratios, which is the fraction of the total photon flux from the upper multiplet E_i that goes to the ground state E_0, and A_i the radiative emission probabilities of each thermalized levels to all multiplets at lower energies. As pointed out by Suta and Meijerink [55], the pre-exponential factor C is usually considered as temperature independent. However, branching ratios and radiative decay rates can be thermally affected when the degeneracies of the thermalized multiplets are broken by the crystal-field into Stark levels, which are not equally populated at low temperatures and the Boltzmann equilibrium between multiplets is not sustained. Only if $k_BT \gg E_{21}$ the population among the Stark levels can be considered in thermal equilibrium and the Boltzmann distribution rules in a practical way, the relative populations of the thermalized multiplets. However, in all practical cases the temperature dependence of C is much weaker than that of the exponential factor in Eq. (1) [55].

When analysing the LIR measurements, it is important to understand which parameters are really sensitive to the nature of the host matrix, i.e., to the nature of the ligands surrounding the optically active Ln^{3+} ion. Since the energy level diagram of the free-Er^{3+} ion is barely independent on the host matrix, when the Er^{3+} ion enter in a certain oxide, fluoride or oxyfluoride local structure in a host matrix, the magnitude of the Ln^{3+}-ligands interaction slightly modifies the energy level diagram by an amount that can be typically of the order of a few tens of cm^{-1}. This crystal-field interaction is of much lower magnitude than the free-Ln^{3+} interactions, which includes electrostatic and spin orbit interactions, and it is considered as a perturbation over the free-Ln^{3+} multiplets, resulting in several Stark levels that depends on the point symmetry of the local site. In summary, the energies of the transition levels involved in the thermal sensor and their energy gaps are expected to be comparable, but not equal, from one matrix to another, as well as the ratio of degeneracies of the thermalized multiplets. Thus the only parameters that strongly depend on the host matrix

7

are the spontaneous emission probabilities A_i [33]. Taking advantage of the Judd-Ofelt theory [51,56], that allows calculating the branching ratios and the radiative absorption and emission probabilities between any two multiplets of a Ln^{3+} ion in a host matrix, the ratio A_{20}/A_{10} can be described as a function of a set of three parameters, $(\Omega_2, \Omega_4, \Omega_6)$ as

$$LIR_{GREEN} = \frac{I_{20}}{I_{10}} \propto \frac{A_{20}}{A_{10}} \cdot e^{-E_{21}/k_BT} = \frac{\beta_{20}}{\beta_{10}} \cdot \frac{A_2}{A_1} \cdot e^{-E_{21}/k_BT}$$

$$\propto \frac{\beta_{20}}{\beta_{10}} \cdot \left(\frac{0.7158\,\Omega_2 + 0.4138\,\Omega_4 + 0.0927\,\Omega_6}{0.2225\,\Omega_6} \right) \cdot e^{-E_{21}/k_BT} \qquad (2)$$

where the (β_{20}/β_{10}) ratio usually ranges from 1 to 1.5 for different host matrices, using the double-reduced matrices of Carnall *et al*. [57] and Weber [58] or those calculated for the YGG garnet by Muñoz-Santiuste [50]. At first glance, those host matrices that may show large Ω_2 and Ω_4 and small Ω_6 parameters would show larger LIR, especially those matrices that show high degree of local distortions of the Er^{3+} environments that results in larger Ω_2 values [33,51,52].

In order to characterize the OTS, it is necessary to provide the rate at which the LIR varies with temperature, known as the absolute thermal sensitivity S_A [33]

$$S_A = \left| \frac{\partial LIR}{\partial T} \right| = LIR \cdot \left(\frac{E_{21}}{kT^2} \right) = \left[C \cdot \left(\frac{E_{21}}{kT^2} \right) \right] \cdot e^{-E_{21}/k_BT} \qquad (3)$$

where C is the pre-exponential factor, and also the relative thermal sensitivity S_R (in % K^{-1})

$$S_R = 100 \cdot \frac{1}{LIR} \left| \frac{\partial LIR}{\partial T} \right| = 100 \cdot \left(\frac{E_{21}}{kT^2} \right) \qquad (4)$$

that only depends on temperature and the energy gap between multiplets, being evident that the larger the energy gap the higher the relative sensitivity. Nonetheless, the larger the energy gap the lower the population and, hence, the LIR values may show larger uncertainties.

The (c_{20}/c_{10}) ratio makes the LIR equation, and the sensitivities, independent of the optical setup used, allowing comparing different Er^{3+}-based OTS. However, the way LIR has been calculated is of paramount importance and it depends on how the I_{10} and I_{20} integrated intensities have been calculated, for which no standard method has been established. Thus, precise comparison between OTS, based on the absolute and the relative sensitivities that are directly related to LIR, is very difficult. The absolute sensitivity S_A is basically related to the emission probabilities and the average energy gap between barycenters, or centres of gravity, of the thermalized multiplets E_{21} (see Eqs. 1 and 3), whereas S_R depends only on this energy gap. In the literature is common to see ranking lists of OTS based on the S_R value, for which E_{21} is normally obtained from the fitting of the experimental LIR to Eq. (1). However, this

fitting may both underestimate or overestimate the energy gap between the $^{2}H_{11/2}$ and $^{4}S_{3/2}$ thermalized multiplets in Er^{3+}-doped systems, e.g. the reported value of $E_{21}=$ 400 cm^{-1} for a silicate glass co-doped with Er^{3+} and Yb^{3+} ions [59] sems unrealistic, unless further comprehensive explanation, since no large changes in the emission energies from the thermalized multiplets are expected among different hosts.

Realistic values of the energy gap E_{21} can only be calculated analysing the free-Er^{3+} ion interaction plus the crystal-field perturbation in each host matrix. These calculations, which give the energies of the multiplets and their Stark levels of Er^{3+} ion, provide a value of $E_{21}=$763 cm^{-1} for the energy gap in YGG crystal (see **Figure 1**) [50], which is quite similar to 762 cm^{-1} in $Y_3Al_5O_{12}$ (YAG), 759 cm^{-1} in $YAlO_3$, 760 cm^{-1} in Y_2O_3, 769 cm^{-1} in Er_2O_3 [50] or 751 cm^{-1} in YVO_4 [60]. However, this energy gap increases up to 804 cm^{-1} if the barycenters, or "centers of gravity", of the Stark levels of each multiplet are considered (see **Figure 1**).

A theoretical LIR calculation can be performed in the framework of the Judd-Ofelt theory [51,56]. The RT absorption spectrum of $(Y_{0.99}Er_{0.01})_3Ga_5O_{12}$, i.e. doped with 1 at.% Er^{3+}, garnet crystal, shown partially in **Figure 2**, presents bands associated with Er^{3+} intra-configurational *4f^{11}-4f^{11}* electronic transitions, starting from $^{4}I_{15/2}$ ground state Stark levels to those of the excited multiplets. Transitions between multiplets have been identified and labelled based on the Dieke's diagram [61] and are electric-dipole in nature, except for the $^{4}I_{13/2}$ first excited state that also have a magnetic-dipole contribution [62]. It is worth noting that sharp peaks confirm that Er^{3+} ions are incorporated in the crystalline garnet structure, and a partial energy level diagram of the Er^{3+} ion in YGG garnet is given in **Figures 1** and **2**.
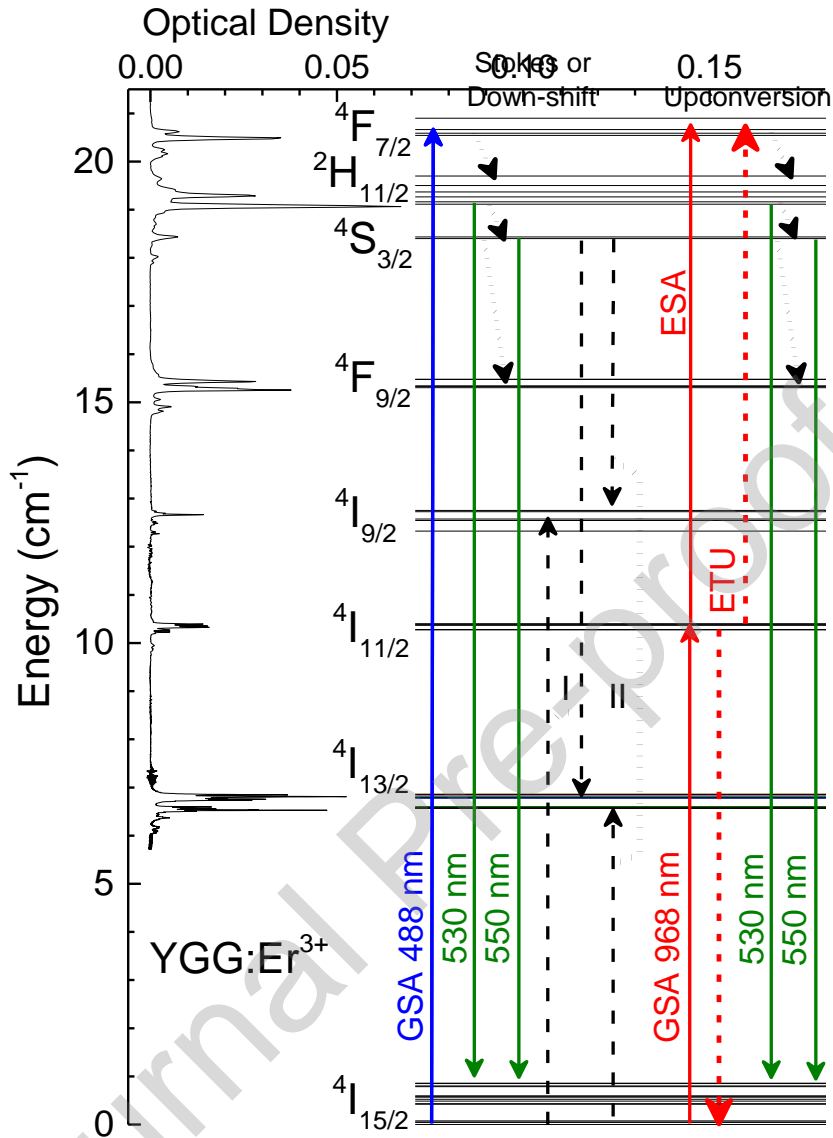
Figure 2. (Left) Partial absorption spectrum of the YGG: Er³⁺ garnet crystal showing the transition energies from the $^4I_{15/2}$ ground state to the excited multiplets. The partial energy level diagram of the Er³⁺ ion incorporates **(middle)** the 488 nm ground state absorption (GSA, blue line), the multiphonon de-excitation channels (black dotted lines) that populate the thermally coupled multiplets, from which the Stokes green luminescence takes place (green lines), along with different cross-relaxation energy transfer processes (in dotted lines and roman numbers). **(Right)** The partial energy level diagram incorporates the 968 nm ground state absorption (GSA, red line), which activates the excited state absorption (ESA, solid red lines) and energy transfer (ETU, dashed red lines) to populate the thermally coupled multiplets, giving rise to the upconverted green luminescence (green lines).

The set of Judd-Ofelt parameters have been calculated using the areas of the absorption bands and the calculated reduced matrix elements [50], and for the Er³⁺ ions in the YGG crystal are found to be (Ω_2=0.93, Ω_4=1.68, Ω_6=0.42 x10⁻²⁰ cm²), which are larger than (Ω_2=0.33, Ω_4=0.26, Ω_6=0.33 x10⁻²⁰ cm²) [63,64], calculated in the same garnet at 700 K but not using the absorption to the $^4I_{13/2}$ due to its large magnetic dipole contribution. With the

10

calculated spontaneous emission probabilities of the $^2H_{11/2}$ (4338 s^{-1}) and $^4S_{3/2}$ (778 s^{-1}) levels to the ground state, the theoretical green LIR of Er^{3+} ions in YGG crystal is

$$LIR = 17.42 \exp(-\frac{763}{K_B T}) \qquad (5)$$

where 763 cm^{-1} is the gap between the $^2H_{11/2}$ and the $^4S_{3/2}$ thermalized levels and it has been obtained from the crystal-field calculations [50], although is quite similar to 804 cm^{-1} calculated with the barycenters, or centres of gravity, of the Stark levels or ~810 cm^{-1} measured from the absorption spectrum (see **Figures 1** and **2**).

Theoretical parameters for the green emissions of Er^{3+} in YGG are presented in **Figure 3**. At RT, LIR has a value of 0.35 and an S_A of 45.5 x 10^{-4} K^{-1}, whereas a maximum value of 80.3 x 10^{-4} K^{-1} is predicted at 583 K, among the highest values found. As it will be discussed later, an overestimation of the radiative probabilities for the $^2H_{11/2}$ and the $^4S_{3/2}$ emitting levels is usually found, due to the calculation process of the Judd-Ofelt parameters, resulting in a larger theoretical LIR than the experimental one. Changes in relative thermal sensitivity are even larger, ranging from 1.23 at RT and rapidly decreasing to 0.11 at 1000 K.

Finally, regarding the temperature uncertainty, δT, this parameter quantifies the smallest temperature change (temperature resolution) that can be achieved in a certain experiment [27]

$$\delta T = \frac{1}{S_R} \cdot \left| \frac{\delta \Delta}{\Delta} \right| \qquad (6)$$

where $\delta\Delta/\Delta$ is the relative uncertainty on Δ calculated using

$$\frac{\delta \Delta}{\Delta} = \sqrt{\left(\frac{\delta I_{10}}{I_{10}}\right)^2 + \left(\frac{\delta I_{20}}{I_{20}}\right)^2} \qquad (7)$$

where $\delta I_{i0}/I_{i0}$ is calculated dividing the readout fluctuations of the baseline by the maximum value of each intensity, i.e., I_{10} and I_{20}. In addition, since the integrated areas are calculated from the same emission spectra it results that $\delta I_{10} = \delta I_{20} = \delta I$.
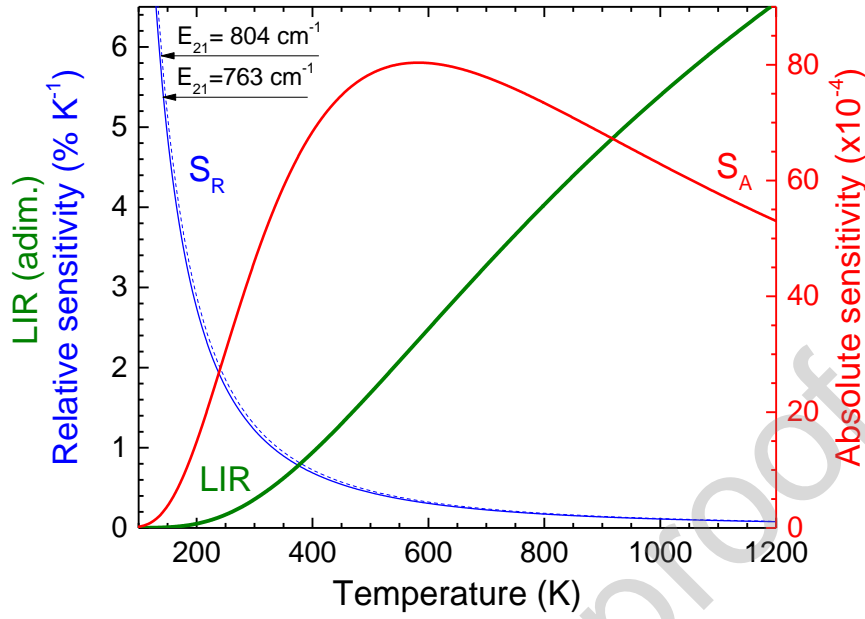
11

Figure 3. Theoretical luminescence intensity ratio (LIR), and absolute (S_A) and relative (S_R) thermal sensitivities for the green thermalized emissions of Er^{3+} in $Y_3Ga_5O_{12}$ garnet crystal.

4. Results and discussion

4.1 Stokes and upconverted luminescence

The RT Stokes, or down-shifted, emission spectrum of YGG: Er^{3+} (1 at.%) under 488 nm laser excitation and a pump power of 13 mW is shown in **Figure 4**. After the resonant absorption of one photon at 488 nm, the Er^{3+} ions are efficiently promoted to the $^4F_{7/2}$ multiplet (see **Figure 2**), from which they decay non-radiatively, mainly due to multiphonon relaxations, populating the $^2H_{11/2}$ and $^4S_{3/2}$ thermalized emitting levels [65]. Emission peaks from the $^4S_{3/2}$ Stark levels are expected but, due to the small energy gap between multiplets, the $^2H_{11/2}$ Stark levels are thermally populated and therefore, emit as well. Absorption and emission of high-energy phonons ($hv_{max} \cong 750$ cm^{-1} in YGG) allow the thermalization to reach a steady-state situation, and both $^2H_{11/2}$ and $^4S_{3/2}$ levels behave as a single level of the Er^{3+} ion with only one de-excitation behaviour (radiative and non-radiative) to the lower states of the $4f^{11}$ ground configuration. Although this study is focused on the $^2H_{11/2},^4S_{3/2} \rightarrow ^4I_{15/2}$ green emissions, there are also important emissions from the $^4F_{9/2}$, (~650 nm), $^4I_{11/2}$ (~975 nm), and $^4I_{15/2}$ (~1530 nm) multiplets to the $^4I_{15/2}$ ground state (not shown). As in absorption, sharp emission peaks confirm the successful incorporation of Er^{3+} ions in the crystalline network.
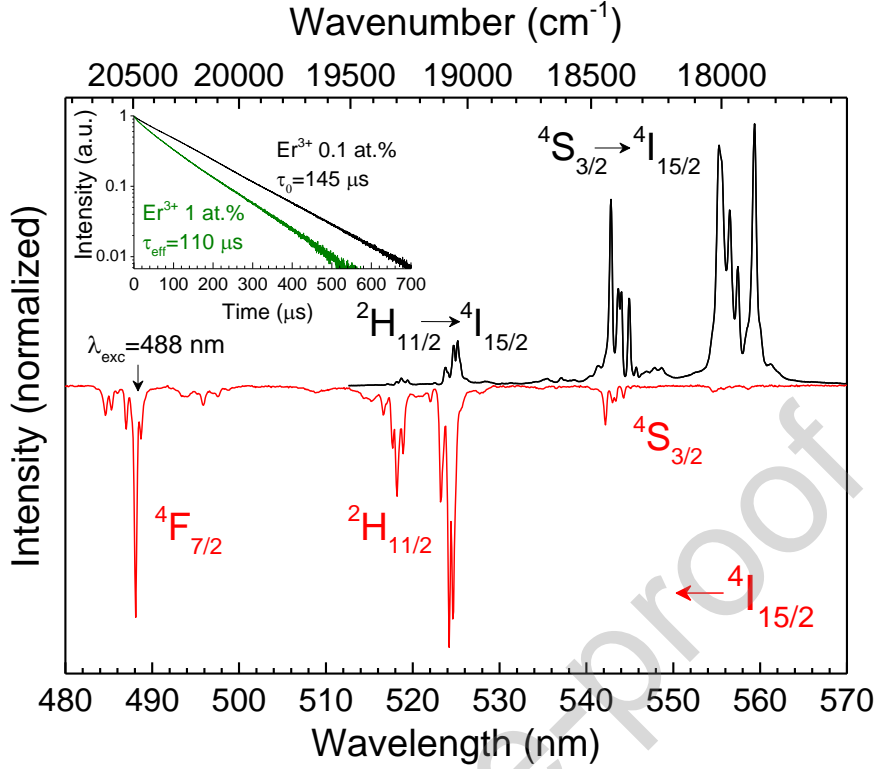
12

Figure 4. Partial absorption (in red) and Stokes emission (in black) spectra of Er^{3+} (1 at.%) in $Y_3Ga_5O_{12}$ garnet crystal. Labels for Er^{3+} transitions are also shown. Inset shows the luminescence decay curves of the thermalized levels under a resonant excitation at 525 nm and monitoring the emission at 555 nm for 0.1 and 1 at.% of Er^{3+}.

Comparison of intensities in the absorption and emission spectra in the visible range, shown in **Figure 4**, clearly highlights the differences in the transition probabilities between the thermalized levels. The $^4I_{15/2} \rightarrow {}^2H_{11/2}$ hypersensitive transition, which has the second highest oscillator strength among all the Er^{3+} intra-configurational transitions in this optical range, is strongly dependent on the Ω_2 Judd-Ofelt parameter. As already mentioned, this parameter is closely related with the nature of the environment of the active ion in the host and, consequently, varies appreciably with the composition [51,52].

The luminescence decay curves of the thermalized levels, exciting resonantly the $^4I_{15/2} \rightarrow {}^2H_{11/2}$ transition at 525 nm and detecting the $^4I_{15/2} \rightarrow {}^4S_{3/2}$ transition at 555 nm, present a concentration-dependent behaviour. Since we are dealing with two thermally-coupled levels, the calculation of the emission lifetimes has to be taken considering an effective radiative lifetime for both multiplets based on Boltzmann distribution:

$$\frac{1}{\tau_{rad}} = \frac{\sum_j \left[g_1 A_{1j} + g_2 A_{2j} \, exp\left(-\frac{E_{21}}{K_B T}\right) \right]}{g_1 + g_2 \, exp\left(-\frac{E_{21}}{K_B T}\right)} \tag{8}$$

13

where the summation extends to all the lower energy j multiplets. From the Judd-Ofelt calculations, a value of $\tau_{rad} \cong 710$ μs has been obtained.

In order to obtain an accurate value for the intrinsic effective lifetime of the thermalized levels, a diluted $(Y_{0.999}Er_{0.001})_3Ga_5O_{12}$ crystal, i.e. doped with 0.1 at.% Er^{3+}, has been synthesized. The luminescence decay curve, given as an inset in **Figure 4**, shows a pure exponential decay curve that, in logarithm scale, is described by a straight line, and the intrinsic lifetime τ_0 $(= \int t \cdot I(t) \cdot dt / \int I(t) \cdot dt)$, which in this case coincides with the time necessary to decay a factor 1/e, is ~145 μs. Taking into account that this lifetime includes the radiative plus the multiphonon de-excitation probabilities, which has to be considered when incorporating the Er^{3+} ions in solids, a rough estimation of the multiphonon relaxation $(W_{MP} = \tau_0^{-1} - \tau_{rad}^{-1})$ from the $(^2H_{11/2}, ^4S_{3/2})$ thermalized levels to the $^4F_{9/2}$ multiplet yields a value of $W_{MP} \cong 5488$ s^{-1}, which is almost 4 times larger than the spontaneous emission probabilities. It is worth noting that the energy transfer contribution to the non-radiative de-excitation probabilities has been discarded due to the low Er^{3+} concentration.

When concentration of Er^{3+} ions is increased ten times, i.e. $(Y_{0.99}Er_{0.01})_3Ga_5O_{12}$ crystal, energy transfer relaxation processes among Er^{3+} ions become important and a decrease in lifetime is observed. Energy transfer is a very fast process, which usually depends on the distance between Er^{3+} ions and the overlapping of its absorption and emission bands [66], and can be easily identified by a non-exponential profile, especially at the early stages of the decay curve, which shows a non-linear behaviour in a logarithm scale (see inset in **Figure 4**). From the temporal evolution of the emission intensity, an estimation of the average lifetime τ $(= \int t \cdot I(t) \cdot dt / \int I(t) \cdot dt)$ can be done, giving a value of ~110 μs. Taken into account all probabilities involved in the de-excitation of the Er^{3+} ions in the thermalized levels and the intrinsic lifetime τ_0, the energy transfer probability can be estimated to be $W_{ET} \cong 2195$ s^{-1} for the YGG garnet crystal doped with 1 at.% of Er^{3+}, around 1.5 times larger than the spontaneous emission probabilities. **Figure 2** shows the most resonant cross-relaxation channels, i.e., channel I $(^4S_{3/2}, ^4I_{15/2} \rightarrow ^4I_{13/2}, ^4I_{9/2})$ and II $(^4S_{3/2}, ^4I_{15/2} \rightarrow ^4I_{9/2}, ^4I_{13/2})$, that are involved in the energy transfer processes of the thermalized levels.

On the other hand, **Figure 5** shows green upconverted emissions of YGG: Er^{3+} (1 at.%), which can be observed by the naked eyes after a resonant 968 nm pump laser excitation of Er^{3+} ions from the $^4I_{15/2}$ ground state to the $^4I_{11/2}$ multiplet. In contrast to down-shifting, upconversion (UC) is a non-linear process in which the optically active ion is initially excited to an intermediate, or reservoir, multiplet to, following a second or more

14

steps, reach the excited emitting levels. Two mechanisms are usually responsible for this process, i.e. the excited state absorption (ESA) and the energy transfer upconversion (ETU) [67]. The former excites the same Er^{3+} ion that is promoted from the ground state to the intermediate level absorbing one photon and, during the same laser pulse, it absorbs another photon to finally reach the excited emitting levels. The ETU mechanism involves energy transfer processes between two physically nearby Er^{3+} ions that have already reached the intermediate level. One of these Er^{3+} ions return to the ground state, providing the transition energy to the second Er^{3+} ion to reach the emitting multiplets. It is worth noting that for a better efficiency of this energy transfer mechanism not only these Er^{3+} ions should be close in distance in the crystal structure, but also the overlapping of the emission and absorption bands of the transitions involved should be as large as possible. Although both mechanisms may contribute to the non-linear UC process, usually one of them dominates [67].
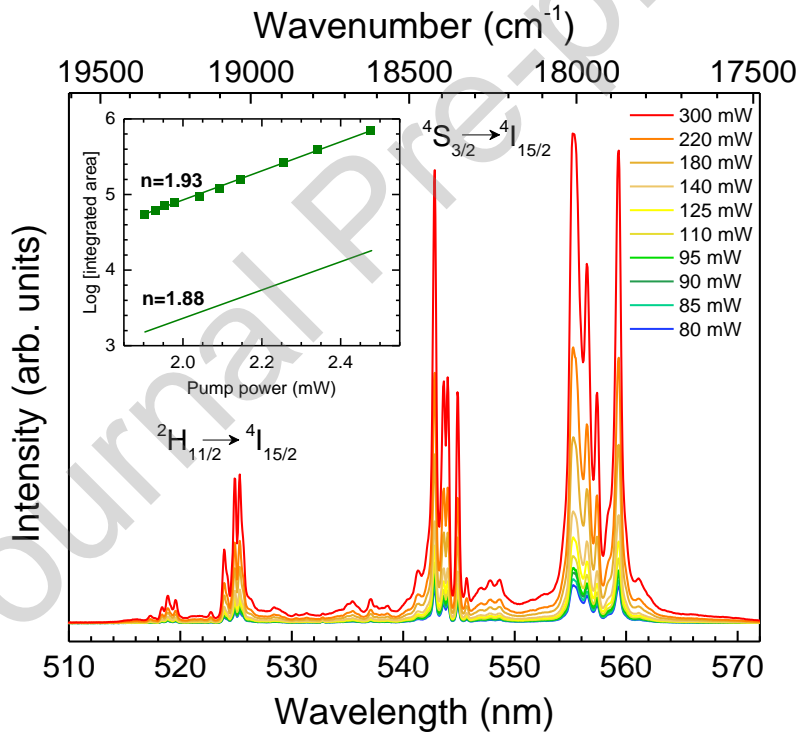

Figure 5. Upconverted emission spectra of Er^{3+} (1 at.%) in $Y_3Ga_5O_{12}$ garnet crystal for different cw 968 nm laser excitation pump powers. Labels for Er^{3+} ion green transitions are also shown. **(Inset)** Pump power dependence of the green upconverted integrated intensity areas in double-log scale for the $^2H_{11/2} \rightarrow {}^4I_{15/2}$, (green hollow squares) and $^4S_{3/2} \rightarrow {}^4I_{15/2}$ (green squares) transitions. Bound between emissions has been taken at 539.2 nm.

Focusing on YGG: Er^{3+} green emission bands related to $^2H_{11/2}, {}^4S_{3/2} \rightarrow {}^4I_{15/2}$ transitions under 968 nm laser excitation, resonant with the $^4I_{15/2} \rightarrow {}^4I_{11/2}$ transition, it can be observed that they are the same as the Stokes emission (see **Figures 4** and **5**). The non-linear nature of the UC processes can be straightforwardly confirmed through the dependence of the green

15

upconverted emission of YGG: Er^{3+} with the cw 968 nm laser pump power, shown in the inset of **Figure 5**. The number of photons involved during the upconversion processes can be estimated according to the expression $I \propto P^n$, where I is the upconverted emission intensity (or the integrated areas of the upconverted emission bands), P is the pump power of the laser excitation and n is the number absorbed photons required to produce an emission photon in the UC processes [67]. According to inset in **Figure 5**, the energy equivalent to two NIR photons is needed to produce the green emissions of Er^{3+} in YGG. This result is well correlated to the UC emission intensity increase as pump power increases (80-300 mW). Slopes are clearly non-quadratic, with values around 1.9, but this effect typically occurs in almost all host matrices, even reaching a linear dependency in the limit of infinitely large UC rates [68].

The energy equivalent to two NIR photons needed in the process can be obtained directly from the laser, as in ESA processes, or one laser photon plus the energy transferred from one Er^{3+} ion in the intermediate, or reservoir, $I_{11/2}$ state that returns to the ground state, as in ETU processes, following the ($^4I_{11/2}$, $^4I_{11/2} \rightarrow ^4I_{15/2}$, $^4F_{7/2}$) cross-relaxation channel (see **Figure 2**). To experimentally test which mechanism is the dominant one, temporal dynamics of the UC processes has been measured after a laser pulse at 968 nm, monitoring the green emission peak at 555 nm. Results, shown in **Figure 6**, are clearly different depending on Er^{3+} concentration. For the low-doped $(Y_{0.999}Er_{0.001})_3Ga_5O_{12}$ crystal, the luminescence decay curves, and the measured lifetimes of the green emissions are the same, independently of the laser excitation, as shown in **Figures 4** and **6**. This indicates that the unique mechanism that rules the UC in this low-doped crystal is ESA, since the whole process occurs during the same laser pulse, exactly the same result when exciting directly in the blue range. However, for the $(Y_{0.99}Er_{0.01})_3Ga_5O_{12}$ crystal, i.e., when the concentration of Er^{3+} ions is increased to 1 at.%, the dynamics of the UC after a laser pulse at 968 nm shows a fast initial rise, just after the laser pulse, followed by a slow increase of the emission intensity up to ~20 µs and then, a slower decrease with time. The initial population is typical of ESA processes while the following rise points to a contribution from a different mechanism, i.e., ETU processes, which feed the green emitting levels. Since intermediate level lifetime is also involved in ETU processes, and it is usually longer than that of the green emitting level, it needs more time to populate the thermalized levels. Thus, it seems that both ESA and ETU mechanisms contribute to the UC in the $(Y_{0.99}Er_{0.01})_3Ga_5O_{12}$ garnet crystal. Analysing the areas under these two temporal evolutions of the intensities in both low- and high-doped crystals, once

16

the maximum of the Er^{3+} low-doped curve has the same magnitude as the initial magnitude of the high-doped one, it is possible to roughly estimate the contribution of each mechanism to the UC processes. Results show that ESA contributes with ~25% to the UC, whereas the dominant mechanism, with a contribution of ~75%, is ETU for the YGG garnet doped with 1 at. % of Er^{3+} ions.
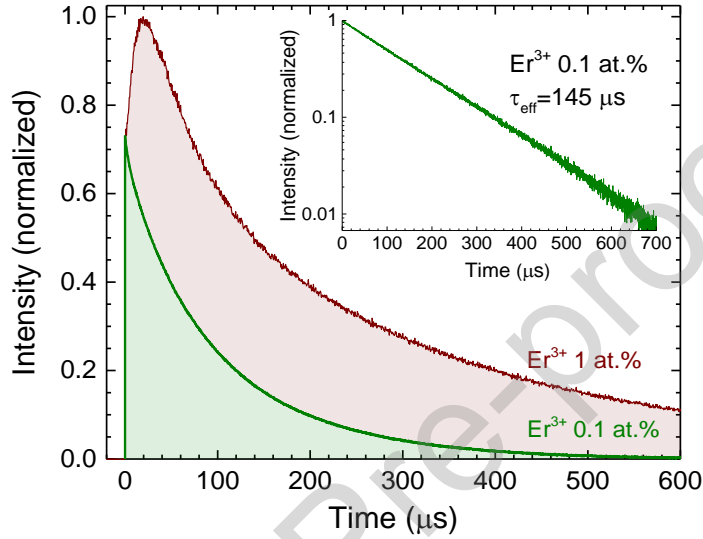

Figure 6. Temporal dynamics of the green luminescence of Er^{3+} ions with 0.1 (green line) and 1 (red-brown line) at. % in $Y_3Ga_5O_{12}$ garnet crystals after a 968 nm pulsed laser excitation. Inset shows the temporal evolution of the low-doped sample in logarithm scale.

4.2 Optical sensor calibration

Green emissions obtained through 488 nm and 968 nm laser excitations of the YGG garnet doped with 1 at. % of Er^{3+} will be employed for the calibration of an OTS working in the visible range and at very high temperatures. The high intensities of the thermalized transitions, the structural stability of YGG garnet at very high temperatures, the negligible influence of black-body radiation, as well as the use of a low-cost, easy setup, using commercially available low-cost lasers and detectors, make this Er^{3+} optically active ion plus garnet crystalline host matrix combination a potential OTS at ultra-high temperatures for industrial applications.

Er^{3+} emission spectra in $(Y_{0.99}Er_{0.01})_3Ga_5O_{12}$ garnet crystal from RT up to 1053 K range under a 13 mW cw 488 nm excitation are shown in **Figure 7 (top)**, whereas the temperature-dependent upconverted green emissions, corresponding to 80 mW 968 nm NIR laser excitation, are also shown in **Figure 7 (bottom)** up to 983 K. In these figures, all spectra have been normalized to the maximum intensity of the $^4S_{3/2} \rightarrow {}^4I_{15/2}$ emission at each temperature. As expected, the emission bands show slight, irrelevant broadening increase with tempera-

17

ture, but without changes or distortions in the Er^{3+} local structure since no energy shifts of emission lines or the appearance of new ones are observed.

As temperature increases, the relative changes in the integrated intensities of the green emissions follows the same rate for both laser excitations: the area of the emission associated with the $^2H_{11/2} \rightarrow {}^4I_{15/2}$ (I_2) hypersensitive transition increases due to the thermally-induced population coming from the $^4S_{3/2}$ lower level, which decreases its intensity (I_1) to the ground state accordingly. This temperature-induced effect can be easily explained by the Boltzmann distribution of population among non-degenerated Stark levels E_i of the $^4S_{3/2}$ and $^2H_{11/2}$ multiplets (see **Figure 1**), given by

$$\frac{N_i}{N} = \frac{e^{-\left(\frac{E_i}{k_b T}\right)}}{\sum_{i=1}^{m} e^{-\left(\frac{E_i}{k_b T}\right)}} \tag{9}$$

in which the lowest Stark level of the $^4S_{3/2}$ multiplet has been taken as the zero of energy. Adding the populations of the Stark levels of each multiplet given by Eq. (9), it has been found a population ratio between multiplets of

$$\frac{N_2(^2H_{11/2})}{N_1(^4S_{3/2})} \cong \frac{6.32 \cdot N}{93.67 \cdot N} \cong 0.07 \quad \text{at RT} \tag{10}$$

$$\frac{N_2(^2H_{11/2})}{N_1(^4S_{3/2})} \cong \frac{50.1 \cdot N}{49.9 \cdot N} \cong 1.004 \quad \text{at 1053 K} \tag{11}$$

The combination of this population ratios and the larger spontaneous emission probability of the upper level, i.e. $A_{20}/A_{10}=5.6$ obtained from the Judd-Ofelt calculations, facilitates the large change of the luminescence intensity ratio between the thermalized green levels of Er^{3+} in YGG garnet with temperature. It is worth noting that in the whole range of temperatures studied, it was possible to measure these green emissions without any disturbance from the black-body radiation of the furnace, although the total intensity of the green emissions decay by two orders of magnitude, probably due to the increase of multiphonon relaxation probability with temperature [55].
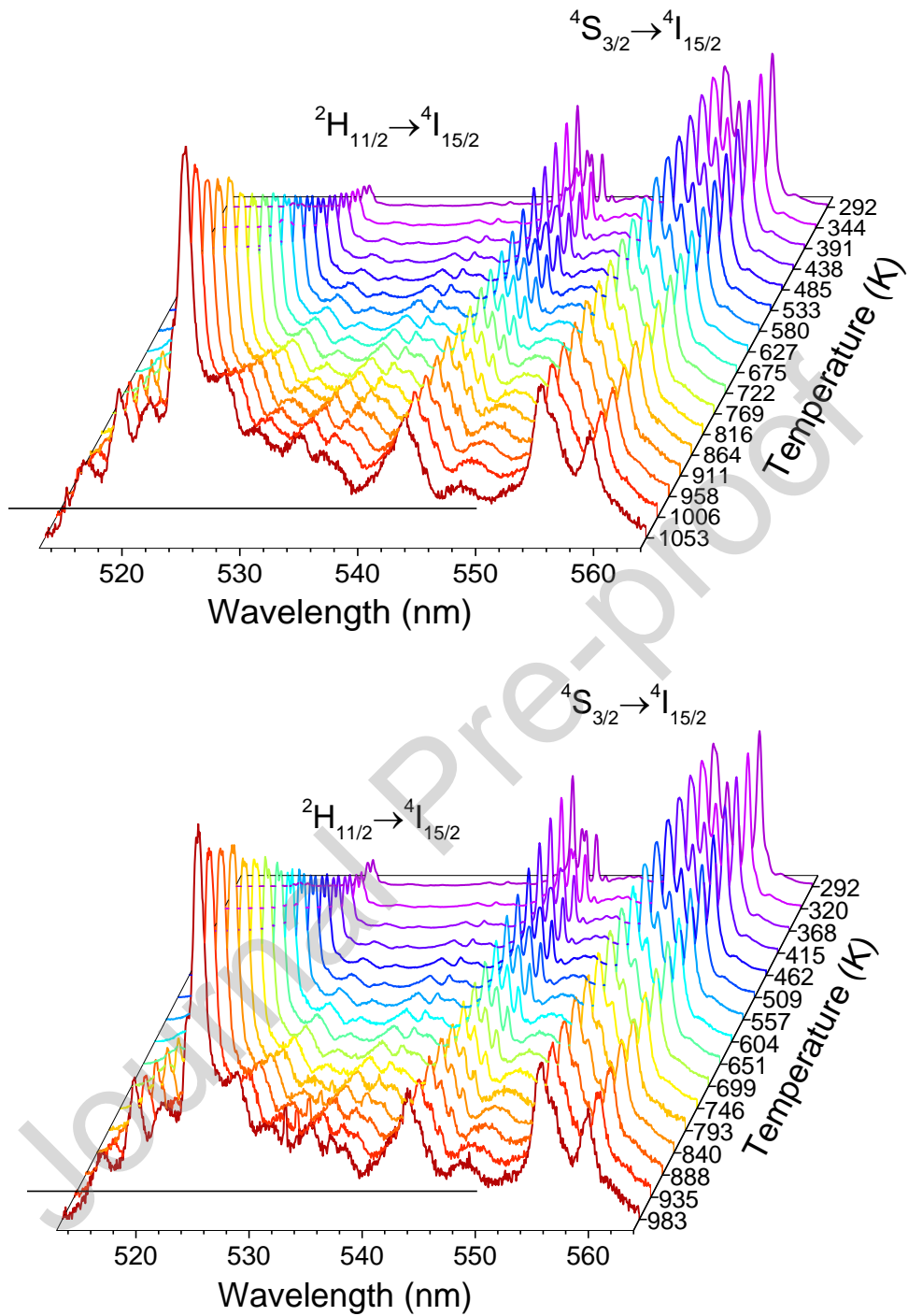
18

Figure 7. Green emission spectra of Er^{3+} ions in $Y_3Ga_5O_{12}$ garnet crystal under (top) 488 nm and (bottom) 968 nm cw laser excitations in the 292-1053 K temperature range. Spectra are normalized to the maximum intensity of the $^4S_{3/2}{\rightarrow}^4I_{15/2}$ emission at each temperature.

This behaviour of I_1 and I_2 with temperature confirm that the LIR=I_1/I_2 is temperature-sensitive, as reported for other Er^{3+}-bearing materials [6,11,69–78]. Since LIR shows the same rate of change with temperature using two different laser excitations in the blue and NIR ranges, data from both experiments have been used to obtain a unique fitting to the

Boltzmann's distribution law given in Eq. (1). The temperature dependence of the experimental data thermometric LIR parameter in the 292-1053 K range is shown in **Figure 8**, in which green filled squares come from the blue laser excitation and green hollow ones from the NIR laser. It is worth noting that, to correctly determine the LIR, the spectra were converted to the energy scale (eV) via the Jacobian transformation [1] and the bound between both emissions was taken at 539.2 nm ($\sim$18546 cm^{-1}). However, two different fittings to Eq. (1) have been developed: a first fitting considering a fixed value of 763 cm^{-1} for the energy gap E_{21} between the thermalized levels, obtained from crystal-field calculations [50], and a second one in which the energy gap is also a free fitting parameter, yielding a final value of 812 cm^{-1}.

According to the fitting result for a fixed energy gap, shown in **Figure 8 (left)**, the values for the pre-exponential factor and the energy gap are C=4.70 and E_{21}=763 cm^{-1}, respectively, and a LIR fit with a $R^2 \cong 0.997$. The thermometric response of the YGG: Er^{3+} garnet crystal was evaluated through the absolute S_A and relative S_R thermal sensitivities with the help of Eqs. (3) and (4), respectively. The maximum absolute sensitivity achieved is $\sim$23.2 x 10^{-4} K^{-1} at 549 K, whereas the maximum relative sensitivity is achieved at RT with a value of $\sim$1.28 %. K^{-1} with an uncertainty in temperature of 1.22 K. However, when the energy gap is allowed to vary in the fitting to Eq. (1), slightly different results are obtained, being C=5.13 and E_{21}=812 cm^{-1}. In the latter calculation, the fitted LIR curve, shown in **Figure 8 (right)**, seems to follow the experimental data slightly better than the first fit, showing a $R^2 \cong 0.999$, and yielding also a slight better pre-exponential value than in the previous fitting procedure that is closer to the theoretical one of 17.42. In addition, the energy gap that is quite close to 804 cm^{-1} obtained from the energy difference between barycenters, or centres of gravity, of the Stark levels of the thermalized levels (see **Figure 1**), and almost the same value as that obtained from the absorption spectrum. This also implies that slightly higher sensitivities are expected, and S_A is $\sim$23.9 x 10^{-4} K^{-1} at 580 K and S_R is $\sim$1.36, with a temperature uncertainty of 1.14 K at RT, comparable to that obtained in the first calculation.
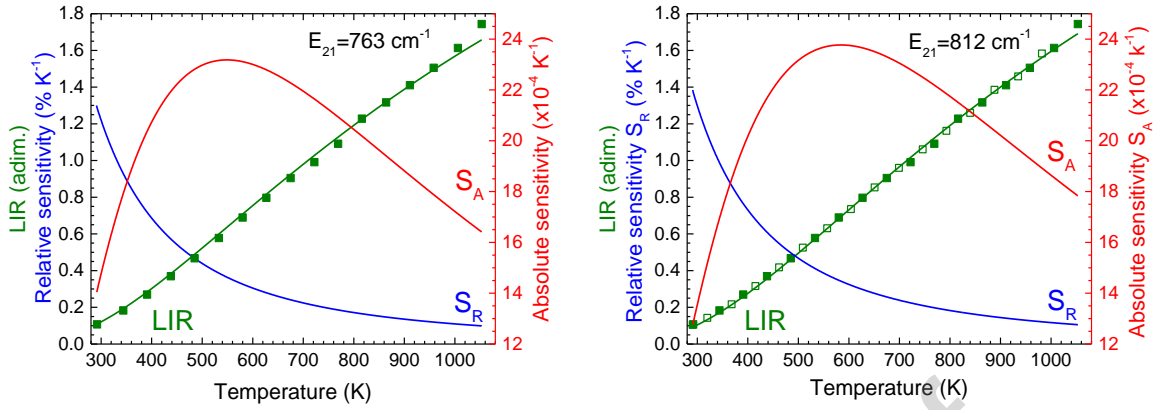
Figure 8. Luminescence intensity ratio (Stokes, green squares; UC, green hollow squares), absolute (red lines) and relative (blue lines) thermal sensitivities and Eq. (1) Boltzmann type fits to the experimental data of LIR (green lines) for an energy gap E_{21} of **(left)** 763 cm^{-1} and **(right)** 812 cm^{-1} (see text).

These results are different from the theoretical ones, obtained by Eq. (5) and shown in **Figure 3**. While relative sensitivities show only slight differences, the experimental absolute sensitivities are clearly smaller than the theoretical one. The difference between the theoretical and experimental calculations, combining the Judd–Ofelt theory and assuming a Boltzmann distribution of population, may have different origins: the increasing overlapping of peaks with temperature, the decreasing signal-to-noise ratio up to two orders of magnitude when 1000 K is reached, compared to RT, and the re-absorption of the emitted photons by other Er^{3+} ions in the ground state that may decrease I_{20} value [31]. All these facts complicate the calculation of I_{10} and I_{20} and its relative changes. On the other hand, an error of ~10-20 % in the Judd-Ofelt theoretical radiative probabilities is generally accepted [51], since the rms method followed in the fitting process depends on the number of experimental oscillator strengths and the values of the double-reduced matrix elements. In fact, it has been already suggested that the use of the Judd–Ofelt theory in the theoretical engineering search for an efficient OTS shows some limitations [33].

Especial attention has to be deserved to the temperature uncertainty. Even though the uncertainty of 1.14 K at RT is high for biological applications, we remind that this is a material whose performance as an OTS is focused on industrial applications, i.e., at very high temperatures, in which extremely high temperature resolution is not necessarily needed. As already mentioned, the relative sensitivity decreases to ~0.1 % K^{-1} at 1000 K, as well as the overall intensity of the green emissions that decreases by two orders of magnitude. These facts have a large influence on the temperature uncertainty, especially the later one since Eq. (7) predicts a large increase when I_{10} and I_{20} intensities decrease. This is clearly reflected in the increase of the temperature uncertainty, which gradually increases from 1.14 K at RT up

21

to 15 K at the highest temperature reached in this experiment of 1050 K. It is worth noting that this temperature uncertainty is still quite good for industrial processing at very high temperatures.
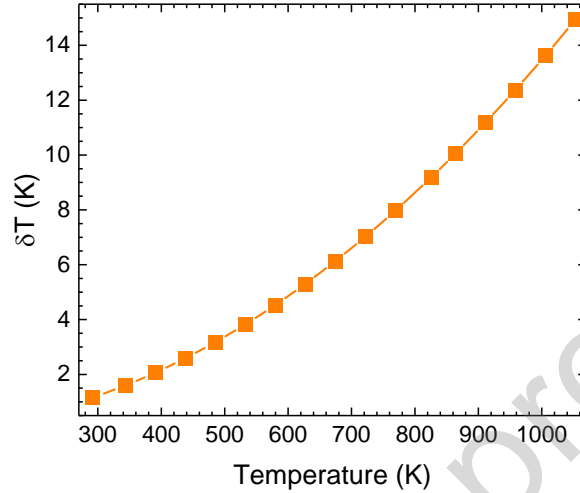

Figure 9. Evolution of the temperature uncertainty from 292 K up to 1053 K.

It is well known that the evaluation and report of the temperature uncertainty is highly demanded in OTS designed for biological applications, requiring high temperature accuracy. For OTS working in high temperature ranges, in which temperature accuracy is not that crucial for industrial applications, such parameter is not commonly reported. In this sense, B. Dong *et al*. reported an OTS based on Al_2O_3: Er^{3+}-Yb^{3+} nanoparticles for high temperature applications with a temperature uncertainty around 0.3 K at 500 K, but obtained from the absolute thermal sensitivity [78]. In 2017, R.G. Geitenbeek *et al*. reported an Er^{3+}-Yb^{3+} co-doped silica-coated upconverting nanocrystals as temperature probe with a temperature accuracy of 1 to 5 K below 750 K [79]. In 2018, M.A. Hernández-Rodríguez *et al*. reported the capabilities of a Er^{3+}-Yb^{3+} ortho-aluminate nanocrystal perovskite as OTS working in the physiological range of temperature as well as high temperature range up to 600 K, exhibiting a temperature uncertainty of 6 K at 600 K [11]. Later on, these authors reported the application of a Er^{3+}-doped yttrium oxysulfate nanophosphor as OTS operating in both physiological and high temperature ranges, showing a maximum temperature uncertainty of 2.5 K at 475 K [6].

Finally, the sensitivity values obtained for the active material under study as an OTS, i.e., ~23 x 10^{-4} K^{-1}, although this value is achieved at ~543 K for an energy gap of 763 cm^{-1} and ~580 K for 812 cm^{-1}, place the YGG: Er^{3+} OTS in the second part of Table 1, in which the sensitive parameters of different Er^{3+}-based OTS are presented. On the other hand, the S_R

22

values, taking 473 K as a common temperature for all samples, were 0.49 %K^{-1} and 0.52 %K^{-1} for the fittings done, respectively. Such values are comparable to the best Er^{3+}-based OTS (see **Table 1**). However, we stress the extension of the YGG:Er^{3+} garnet crystal operative temperature range (~1000 K), which is higher compared to many other sensors found in the literature (see **Figure 10**), and could be increased up to 2300 K. Comparing these results, it can be concluded that Y$_3$Ga$_5$O$_{12}$:Er^{3+} garnet crystal displays high temperature accuracy in a wider temperature range and can be an excellent candidate as optical high temperature sensor for industrial applications.

Table 1. Excitation wavelength (λ_{exc}, nm), temperature range (ΔT, K), thermally coupled levels energy gap (E_{21}, cm^{-1}), the preexponential factor (C), the maximum absolute thermal sensitivity (S_A, x10^{-4} K^{-1}) and the relative sensitivity at 473 K (S_R, %K^{-1}) of illustrative Er^{3+}- based optical temperature sensors involving the ratio of the emission integrated areas of the Er^{3+} emissions associated to the $^2H_{11/2} \rightarrow {}^4I_{15/2}$ and $^4S_{3/2} \rightarrow {}^4I_{15/2}$ transitions.

Er^{3+}-doped materials	λ_{exc}	ΔT	E_{21}	C	S_A (at T, in K)	S_R	Ref.
2CaO.Al$_2$O$_3$ glass: Er^{3+}	980	150-762	899	37.97	160.05 (642)	0.57	[29]
BiOCl: Er^{3+}	980	298-778	864	6.51	28.55 (617)	0.55	[69]
BaGdF$_5$: Er^{3+} glass ceramic	980	300-720	859	4.78	21.09 (614)	0.55	[80]
YGG: Er^{3+} nanogarnet	488-800	300-850	850	8.21	36.60 (607)	0.54	[81]
YGG: Er^{3+} garnet crystal	488, 968	292-1053	812	5.13	23.94 (580)	0.52	This work
YGG: Er^{3+} garnet crystal*	488, 968	292-1053	763	4.70	23.34 (545)	0.49	This work
YAP: Er^{3+}-Yb^{3+} nanoperovskite	980	296–600	751	5.77	29.11 (536)	0.48	[11]
NaYF$_4$: SiO$_2$: Yb^{3+}- Er^3 nanocrystal	980	300-900	716	9.4	49.75 (512)	0.46	[79]
BaMoO$_4$: Yb^{3+}- Er^{3+}	980	298-573	686	20.06	110.81 (490)	0.44	[70]
Y$_2$O$_2$SO$_4$: Er^{3+}	975	295-473	675	13.02	73.07 (473)	0.43	[6]
Al$_2$O$_3$: Er^{3+}-Yb^{3+} nanoparticles	978	295–975	675	9.63	54.06 (482)	0.43	[78]
Silicate glass: Er^{3+}– Yb^{3+}	978	296-723	415	3.65	33.33 (296)	0.27	[59]

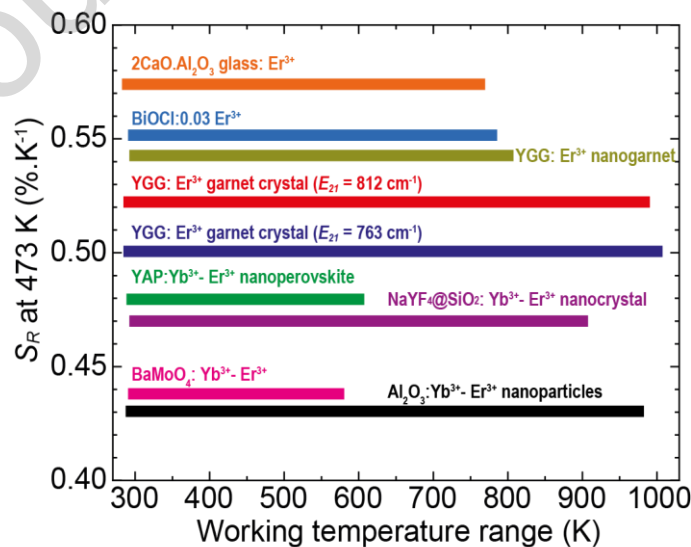*The value of the energy gap was fixed to 763 cm^{-1} in the fitting process.

Figure 10. Comparison of the relative sensitivity S_R at 473 K and working temperature range of some representative Er^{3+}- based optical temperature sensors.

Conclusions

Temperature dependence of the green emissions of Er^{3+} ions in $Y_3Ga_5O_{12}$ garnet crystal were studied under 488 and 968 nm laser excitations. A calibration of the relative intensities of the green emissions from the $^2H_{11/2}$ and $^4S_{3/2}$ thermally-coupled multiplets to the $^4I_{15/2}$ ground state were calibrated within temperature range from 292 K up to, and beyond, 1000 K. The temperature scale obtained from the calibration procedure revealed a maximum in the absolute thermal sensitivity of ~23.9 x 10^{-4} K^{-1} at 580 K and a relative thermal sensitivity of ~1.36 %K^{-1} at RT, combining results for both laser excitations. Comparison of the performance of Er^{3+}-doped $Y_3Ga_5O_{12}$ garnet crystal with other Er^{3+}-based optical temperature sensors, and considering its outstanding advantages, such as a long-working temperature range with a physical upper limit of ~2000 K, capability to be synthesized in cylindrical bulk, prismatic pixel array and fiber forms, a stable structure up to 2300 K, a negligible black-body radiation interference, as well as a low-cost, basic setup, using commercially available low-cost lenses, lasers and detectors, strongly support the Er^{3+}-doped $Y_3Ga_5O_{12}$ garnet crystal as an excellent candidate optical temperature sensor, exhibiting large sensitivity and good temperature resolution for ultra-high temperature industrial applications.

CRediT authorship contribution statement

M.A. Hernández-Rodríguez: Conceptualization, Investigation, Formal analysis, Writing – original draft & Writing – review and editing.

K. Kamada & A. Yoshikawa: Resources

J.E. Muñoz-Santiuste: Resources, Methodology, Software & Formal analysis

A. Casasnovas-Melián: Formal analysis

I.R. Martín, U.R. Rodríguez-Mendoza & V. Lavín: Conceptualization, Supervision & Writing – review and editing.

Conflicts of interest

There are no conflicts of interest to declare.

Acknowledgements

References

[1]   C.D.S. Brites, S. Balabhadra, L.D. Carlos, Lanthanide- Based Thermometers: At the Cutting- Edge of Luminescence Thermometry, Adv. Opt. Mater. 7 (2019) 1801239. https://doi.org/10.1002/adom.201801239.

[2]   Global Market Insights, Inc., (n.d.). www.gminsights.com.

[3]   Durex Industries, (n.d.). www.durexindustries.com.

[4]   Ametherm, (n.d.). www.ametherm.com.

[5]   D. Erwin, Summary for Policymakers, in: Intergovernmental Panel on Climate Change (Ed.), Clim. Chang. 2013 - Phys. Sci. Basis, Cambridge University Press, Cambridge, 2015: pp. 1–30. https://doi.org/10.1017/CBO9781107415324.004.

[6]   M.A. Hernández-Rodríguez, P. Tadge, A.D. Lozano-Gorrín, U.R. Rodríguez-Mendoza, S. Ray, V. Lavín, Upconversion and luminescence temperature sensitivity of Er^{3+} ions in yttrium oxysulfate nanophosphor, Opt. Mater. 95 (2019) 109197. https://doi.org/10.1016/j.optmat.2019.109197.

[7]   A.D. Lozano-Gorrín, U.R. Rodríguez-Mendoza, V. Venkatramu, V. Monteseguro, M.A. Hernández-Rodríguez, I.R. Martín, V. Lavín, Lanthanide-doped $Y_3Ga_5O_{12}$ garnets for nanoheating and nanothermometry in the first biological window, Opt. Mater. 84 (2018) 46–51. https://doi.org/10.1016/j.optmat.2018.06.043.

[8]   L. García-Rodríguez, L. de Sousa-Vieira, M.A. Hernández-Rodríguez, A.D. Lozano-Gorrín, V. Lavín, U.R. Rodríguez-Mendoza, J. González-Platas, S. Ríos, I.R. Martín, Nanoperovskite doped with Yb^{3+} and Tm^{3+} ions used as an optical upconversion temperature sensor, Opt. Mater. 83 (2018) 187–191. https://doi.org/10.1016/j.optmat.2018.06.009.

[9]   M.A. Hernández-Rodríguez, A.D. Lozano-Gorrín, I.R. Martín, U.R. Rodríguez-Mendoza, V. Lavín, Comparison of the sensitivity as optical temperature sensor of nano-perovskite doped with Nd^{3+} ions in the first and second biological windows, Sensors Actuators B Chem. 255 (2018) 970–976. https://doi.org/10.1016/j.snb.2017.08.140.

[10]   M.A. Hernández- Rodríguez, A.D. Lozano-Gorrín, V. Lavín, U.R. Rodríguez-Mendoza, I.R. Martín, Yttrium orthoaluminate nanoperovskite doped with Tm^{3+} ions as upconversion optical temperature sensor in the near-infrared region, Opt. Express. 25 (2017) 27845. https://doi.org/10.1364/OE.25.027845.

[11] M.A. Hernández- Rodríguez, A.D. Lozano-Gorrín, V. Lavín, U.R. Rodríguez-Mendoza, I.R. Martín, F.J. Manjón, Analysis of the upconversion emission of yttrium orthoaluminate nano-perovskite co-doped with Er^{3+}/Yb^{3+}ions for thermal sensing applications, J. Lumin. 202 (2018) 316–321. https://doi.org/10.1016/j.jlumin.2018.05.078.

[12] M. Runowski, P. Woźny, I.R. Martín, V. Lavín, S. Lis, Praseodymium doped $YF_3:Pr^{3+}$ nanoparticles as optical thermometer based on luminescence intensity ratio (LIR) – Studies in visible and NIR range, J. Lumin. 214 (2019) 116571. https://doi.org/10.1016/j.jlumin.2019.116571.

[13] M. Runowski, A. Bartkowiak, M. Majewska, I.R. Martín, S. Lis, Upconverting lanthanide doped fluoride $NaLuF_4:Yb^{3+}-Er^{3+}-Ho^{3+}$ - optical sensor for multi-range fluorescence intensity ratio (FIR) thermometry in visible and NIR regions, J. Lumin. 201 (2018) 104–109. https://doi.org/10.1016/j.jlumin.2018.04.040.

[14] M. Runowski, P. Woźny, V. Lavín, S. Lis, Optical pressure nano-sensor based on lanthanide doped $SrB_2O_4:Sm^{2+}$ luminescence – Novel high-pressure nanomanometer, Sensors Actuators B Chem. 273 (2018) 585–591. https://doi.org/10.1016/j.snb.2018.06.089.

[15] M. Runowski, Pressure and temperature optical sensors: luminescence of lanthanide-doped nanomaterials for contactless nanomanometry and nanothermometry, in: Handb. Nanomater. Anal. Chem., Elsevier, 2020: pp. 227–273. https://doi.org/10.1016/B978-0-12-816699-4.00010-4.

[16] M.A. Hernández-Rodríguez, U.R. Rodríguez-Mendoza, V. Lavín, J.E. Muñoz-Santiuste, I.R. Martín, A.D. Lozano-Gorrín, High pressure sensitivity of anti-Stokes fluorescence in Nd^{3+} doped yttrium orthoaluminate nano-perovskites, J. Lumin. 196 (2018) 20–24. https://doi.org/10.1016/j.jlumin.2017.12.008.

[17] M.A. Hernández-Rodríguez, J.E. Muñoz-Santiuste, V. Lavín, A.D. Lozano-Gorrín, P. Rodríguez-Hernández, A. Muñoz, V. Venkatramu, I.R. Martín, U.R. Rodríguez-Mendoza, High pressure luminescence of Nd^{3+} in YAlO 3 perovskite nanocrystals: A crystal-field analysis, J. Chem. Phys. 148 (2018) 044201. https://doi.org/10.1063/1.5010150.

[18] M. Runowski, P. Woźny, N. Stopikowska, Q. Guo, S. Lis, Optical Pressure Sensor Based on the Emission and Excitation Band Width (fwhm) and Luminescence Shift of Ce^{3+} -Doped Fluorapatite—High-Pressure Sensing, ACS Appl. Mater. Interfaces. 11 (2019) 4131–4138. https://doi.org/10.1021/acsami.8b19500.

[19] D. Jaque, F. Vetrone, Luminescence nanothermometry, Nanoscale. 4 (2012) 4301–26. https://doi.org/10.1039/c2nr30764b.

[20] S. Pal, J. Mandal, T. Sun, K.T.V. Grattan, M. Fokine, F. Carlsson, P.Y. Fonjallaz, S.A. Wade, S.F. Collins, Characteristics of potential fibre Bragg grating sensor-based devices at elevated temperatures, Meas. Sci. Technol. (2003). https://doi.org/10.1088/0957-0233/14/7/331.

[21] T.L. Lowder, K.H. Smith, B.L. Ipson, A.R. Hawkins, R.H. Selfridge, S.M. Schultz, High-temperature sensing using surface relief fiber Bragg gratings, IEEE Photonics Technol. Lett. 17 (2005) 1926–1928. https://doi.org/10.1109/LPT.2005.852646.

[22] T. Zhu, T. Ke, Y. Rao, K.S. Chiang, Fabry–Perot optical fiber tip sensor for high temperature measurement, Opt. Commun. 283 (2010) 3683–3685. https://doi.org/10.1016/j.optcom.2010.05.037.

[23] T. Habisreuther, T. Elsmann, Z. Pan, A. Graf, R. Willsch, M.A. Schmidt, Sapphire fiber Bragg gratings for high temperature and dynamic temperature diagnostics, Appl. Therm. Eng. 91 (2015) 860–865. https://doi.org/10.1016/j.applthermaleng.2015.08.096.

[24] D. Jaque, L. Martínez Maestro, B. del Rosal, P. Haro-González, A. Benayas, J.L. Plaza, E. Martín Rodríguez, J. García Solé, Nanoparticles for photothermal therapies, Nanoscale. 6 (2014) 9494–9530. https://doi.org/10.1039/C4NR00708E.

[25] V.K. Rai, Temperature sensors and optical sensors, Appl. Phys. B. 88 (2007) 297–303. https://doi.org/10.1007/s00340-007-2717-4.

[26] S.A. Wade, S.F. Collins, G.W. Baxter, Fluorescence intensity ratio technique for optical fiber point temperature sensing, J. Appl. Phys. 94 (2003) 4743–4756. https://doi.org/10.1063/1.1606526.

[27] C.D.S. Brites, A. Millán, L.D. Carlos, Lanthanides in Luminescent Thermometry, in: Handb. Phys. Chem. Rare Earths, 2016: pp. 339–427. https://doi.org/10.1016/bs.hpcre.2016.03.005.

[28] E.A. Lalla, A.D. Lozano-Gorrín, M. Konstantinidis, M. Daly, S.F. León-Luis, V. Lavín, U.R. Rodríguez-Mendoza, Optical temperature sensor based on Sm^{3+} emissions in a fluorotellurite glass, Opt. Fiber Technol. 47 (2019) 178–186. https://doi.org/10.1016/j.yofte.2018.12.005.

[29] S.F. León-Luis, V. Monteseguro, U.R. Rodríguez-Mendoza, I.R. Martín, D. Alonso, J.M. Cáceres, V. Lavín, $2CaO \cdot Al_2O_3 : Er^{3+}$ glass: An efficient optical temperature sensor, J. Lumin. 179 (2016) 272–279. https://doi.org/10.1016/j.jlumin.2016.07.005.

[30] E.A. Lalla, S.F. León-Luis, V. Monteseguro, C. Pérez-Rodríguez, J.M. Cáceres, V. Lavín, U.R. Rodríguez-Mendoza, Optical temperature sensor based on the Nd^{3+} infrared thermalized emissions in a fluorotellurite glass, J. Lumin. 166 (2015) 209–214. https://doi.org/10.1016/j.jlumin.2015.05.029.

[31] S.F. León-Luis, U.R. Rodríguez-Mendoza, I.R. Martín, E. Lalla, V. Lavín, Effects of Er^{3+} concentration on thermal sensitivity in optical temperature fluorotellurite glass sensors, Sensors Actuators, B Chem. 176 (2013) 1167–1175. https://doi.org/10.1016/j.snb.2012.09.067.

[32] N. Vijaya, P. Babu, V. Venkatramu, C.K. Jayasankar, S.F. León-Luis, U.R. Rodríguez-Mendoza, I.R. Martín, V. Lavín, Optical characterization of Er^{3+}-doped zinc fluorophosphate glasses for optical temperature sensors, Sensors Actuators, B Chem. 186 (2013) 156–164. https://doi.org/10.1016/j.snb.2013.05.081.

[33] S.F. León-Luis, U.R. Rodríguez-Mendoza, P. Haro-González, I.R. Martín, V. Lavín, Role of the host matrix on the thermal sensitivity of Er^{3+} luminescence in optical temperature sensors, Sensors Actuators B Chem. 174 (2012) 176–186. https://doi.org/10.1016/j.snb.2012.08.019.

[34] M. Runowski, P. Wozny, N. Stopikowska, I.R. Martín, V. Lavín, S. Lis, Luminescent nanothermometer operating at very high temperature-sensing up to 1000 K with upconverting nanoparticles (Yb^{3+}/Tm^{3+}), ACS Appl. Mater. Interfaces. 12 (2020) 43933–43941. https://doi.org/10.1021/acsami.0c13011.

[35] K. Kamada, T. Endo, K. Tsutumi, T. Yanagida, Y. Fujimoto, A. Fukabori, A. Yoshikawa, J. Pejchal, M. Nikl, Composition Engineering in Cerium-Doped $(Lu,Gd)_3$ $(Ga,Al)_5O_{12}$ Single-Crystal Scintillators, Cryst. Growth Des. 11 (2011) 4484–4490. https://doi.org/10.1021/cg200694a.

[36] K. Kamada, Y. Shoji, V. V. Kochurikhin, S. Okumura, S. Yamamoto, A. Nagura, J.Y. Yeom, S. Kurosawa, Y. Yokota, Y. Ohashi, M. Nikl, A. Yoshikawa, Growth and scintillation properties of 3 in. diameter Ce doped $Gd_3Ga_3Al_2O_{12}$ scintillation single crystal, J. Cryst. Growth. 452 (2016) 81–84. https://doi.org/10.1016/j.jcrysgro.2016.04.037.

[37] M. Nikl, A. Yoshikawa, K. Kamada, K. Nejezchleb, C.R. Stanek, J.A. Mares, K. Blazek, Development of LuAG-based scintillator crystals – A review, Prog. Cryst. Growth Charact. Mater. 59 (2013) 47–72.

https://doi.org/10.1016/j.pcrysgrow.2013.02.001.

[38] A. Yoshikawa, V. Chani, Growth of Optical Crystals by the Micro-Pulling-Down Method, MRS Bull. 34 (2009) 266–270. https://doi.org/10.1557/mrs2009.77.

[39] A. Djebli, F. Boudjada, K. Pauwels, V. Kononets, G. Patton, A. Benaglia, M. Lucchini, F. Moretti, O. Sidletskiy, C. Dujardin, P. Lecoq, E. Auffray, K. Lebbou, Growth and characterization of Ce-doped YAG and LuAG fibers, Opt. Mater. 65 (2017) 66–68. https://doi.org/10.1016/j.optmat.2016.09.028.

[40] C. Dujardin, E. Auffray, E. Bourret-Courchesne, P. Dorenbos, P. Lecoq, M. Nikl, A.N. Vasil'ev, A. Yoshikawa, R.-Y. Zhu, Needs, Trends, and Advances in Inorganic Scintillators, IEEE Trans. Nucl. Sci. 65 (2018) 1977–1997. https://doi.org/10.1109/TNS.2018.2840160.

[41] J.S. Abell, I.R. Harris, B. Cockayne, B. Lent, An investigation of phase stability in the Y2O3-Al2O3 system, J. Mater. Sci. 9 (1974) 527–537. https://doi.org/10.1007/BF00551870.

[42] V.F. Popova, A.G. Petrosyan, E.A. Tugova, D.P. Romanov, V. V. Gusarov, Y_2O_3-Ga_2O_3 phase diagram, Russ. J. Inorg. Chem. 54 (2009) 624–629. https://doi.org/10.1134/S0036023609040202.

[43] M. Frede, R. Wilhelm, M. Brendel, C. Fallnich, F. Seifert, B. Willke, K. Danzmann, High power fundamental mode Nd:YAG laser with efficient birefringence compensation, Opt. Express. 12 (2004) 3581. https://doi.org/10.1364/OPEX.12.003581.

[44] M.T. Lucchini, K. Pauwels, K. Blazek, S. Ochesanu, E. Auffray, Radiation Tolerance of LuAG:Ce and YAG:Ce Crystals Under High Levels of Gamma- and Proton-Irradiation, IEEE Trans. Nucl. Sci. 63 (2016) 586–590. https://doi.org/10.1109/TNS.2015.2493347.

[45] A. Yoshikawa, B.M. Epelbaum, K. Hasegawa, S.D. Durbin, T. Fukuda, Microstructures in oxide eutectic fibers grown by a modified micro-pulling-down method, J. Cryst. Growth. 205 (1999) 305–316. https://doi.org/10.1016/S0022-0248(99)00265-1.

[46] Yoshikawa A., Oxide Eutectic Crystals for High-Temperature Structural Application, in: F. T., R. P., U. S. (Eds.), Fiber Cryst. Growth from Melt. Adv. Mater. Res. Vol 6., Springer, Berlin, Heidelberg, 2004: pp. 185–217. https://doi.org/https://doi.org/10.1007/978-3-662-07214-1_6.

[47] A. Yoshikawa, M. Nikl, G. Boulon, T. Fukuda, Challenge and study for developing of novel single crystalline optical materials using micro-pulling-down method, Opt. Mater. 30 (2007) 6–10. https://doi.org/10.1016/j.optmat.2006.10.030.

[48] Pawlak D.A., Eutectic Fibers with Self-Organized Structures, in: F. T., C. V.I. (Eds.), Shaped Crystals. Adv. Mater. Res. Vol 8, Springer, Berlin, Heidelberg, 2007: pp. 129–139. https://doi.org/https://doi.org/10.1007/978-3-540-71295-4_8.

[49] A.R. Edmonds, Spectroscopic Properties of Rare Earths, Opt. Acta Int. J. Opt. 12 (1965) 413–413. https://doi.org/10.1080/715120855.

[50] J.E. Muñoz-Santiuste, Crystal-field calculation program, (n.d.) Universidad Carlos III de Madrid, Spain.

[51] R.D. Peacock, The intensities of lanthanide f $\leftrightarrow$ f transitions, in: Rare Earths, Springer Berlin Heidelberg, Berlin, Heidelberg, 1975: pp. 83–122. https://doi.org/10.1007/BFb0116556.

[52] C. Görller-Walrand, K. Binnemans, Spectral intensities of f-f transitions, in: Opt. Mater., 1998: pp. 101–264. https://doi.org/10.1016/S0168-1273(98)25006-9.

[53] C.D.S. Brites, P.P. Lima, N.J.O. Silva, A. Millán, V.S. Amaral, F. Palacio, L.D. Carlos, Thermometry at the nanoscale, Nanoscale. 4 (2012) 4799–4829. https://doi.org/10.1039/c2nr30663h.

[54] B. del Rosal, E. Ximendes, U. Rocha, D. Jaque, In Vivo Luminescence Nanothermom-

etry: from Materials to Applications, Adv. Opt. Mater. 5 (2017) 1600508. https://doi.org/10.1002/adom.201600508.

[55] M. Suta, A. Meijerink, A Theoretical Framework for Ratiometric Single Ion Lumines-cent Thermometers—Thermodynamic and Kinetic Guidelines for Optimized Perfor-mance, Adv. Theory Simulations. 3 (2020) 2000176. https://doi.org/10.1002/adts.202000176.

[56] B.R. Judd, Optical Absorption Intensities of Rare-Earth Ions, Phys. Rev. 127 (1962) 750–761. https://doi.org/10.1103/PhysRev.127.750.

[57] W.T. Carnall, H. Crosswhite, H.M. Crosswhite, Energy level structure and transition probabilities in the spectra of the trivalent lanthanides in LaF_3 , Argonne, IL (United States), 1978. https://doi.org/10.2172/6417825.

[58] M.J. Weber, Probabilities for Radiative and Nonradiative Decay of Er^{3+} in LaF3, Phys. Rev. 157 (1967) 262–272. https://doi.org/10.1103/PhysRev.157.262.

[59] C. Li, B. Dong, S. Li, C. Song, Er^{3+}–Yb^{3+} co-doped silicate glass for optical tempera-ture sensor, Chem. Phys. Lett. 443 (2007) 426–429. https://doi.org/10.1016/j.cplett.2007.06.081.

[60] J.A. Capobianco, P. Kabro, F.S. Ermeneux, R. Moncorgé, M. Bettinelli, E. Cavalli, Optical spectroscopy, fluorescence dynamics and crystal-field analysis of Er^{3+} in YVO4, Chem. Phys. 214 (1997) 329–340. https://doi.org/10.1016/S0301-0104(96)00318-7.

[61] G.H. Dieke, R.A. Satten, Spectra and Energy Levels of Rare Earth Ions in Crystals, Am. J. Phys. 38 (1970) 399–400. https://doi.org/10.1119/1.1976350.

[62] W.T. Carnall, P.R. Fields, K. Rajnak, Electronic Energy Levels in the Trivalent Lan-thanide Aquo Ions. I. Pr^{3+} , Nd^{3+} , Pm^{3+} , Sm^{3+} , Dy^{3+} , Ho^{3+} , Er^{3+} , and Tm^{3+}, J. Chem. Phys. 49 (1968) 4424–4442. https://doi.org/10.1063/1.1669893.

[63] A.A. Kaminskii, A.G. Petrosyan, G.A. Denisenko, T.I. Butaeva, V.A. Fedorov, S.E. Sarkisov, Spectroscopic properties and 3 μm stimulated emission of Er^{3+} ions in the $(Y_{1-x}Er_x)_3Al_5O_{12}$ and $(Lu_{1-x}Er_3)_3Al_5O_{12}$ garnet crystal systems, Phys. Status Solidi. 71 (1982) 291–312. https://doi.org/10.1002/pssa.2210710202.

[64] J.R. Chamberlain, A.C. Everitt, J.W. Orton, Optical absorption intensities and quantum counter action of Er^{3+} in yttrium gallium garnet, J. Phys. C Solid State Phys. 1 (1968) 318. https://doi.org/10.1088/0022-3719/1/1/318.

[65] S. Tamura, I. Hasegawa, N. Imanaka, T. Maekawa, T. Tsumiishi, K. Suzuki, H. Ishi-kawa, A. Ikeshima, Y. Kawabata, N. Sakita, G. Adachi, Carbon dioxide gas sensor based on trivalent cation and divalent oxide anion conducting solids with rare earth oxycarbonate based auxiliary electrode, Sensors Actuators B Chem. 108 (2005) 359–363. https://doi.org/10.1016/j.snb.2004.11.080.

[66] B. Di Bartolo, Energy transfer among ions in solids, in: B. Di Bartolo (Ed.), Energy Transf. Process. Condens. Matter, NATO ASI SERIES, Plenum Press, New York, 1984: pp. 103–203.

[67] F. Auzel, Upconversion and Anti-Stokes Processes with f and d Ions in Solids, Chem. Rev. 104 (2004) 139–174. https://doi.org/10.1021/cr020357g.

[68] M. Pollnau, D.R. Gamelin, S.R. Lüthi, H.U. Güdel, M.P. Hehlen, Power dependence of upconversion luminescence in lanthanide and transition-metal-ion systems, Phys. Rev. B. 61 (2000) 3337–3346. https://doi.org/10.1103/PhysRevB.61.3337.

[69] P. Du, L. Luo, J.S. Yu, Tunable color upconverison emissions in erbium(III)-doped BiOCl microplates for simultaneous thermometry and optical heating, Microchim. Ac-ta. 184 (2017) 2661–2669. https://doi.org/10.1007/s00604-017-2278-0.

[70] X. Liu, R. Lei, F. Huang, D. Deng, H. Wang, S. Zhao, S. Xu, Dependence of upcon-version emission and optical temperature sensing behavior on excitation power in

Er^{3+}/Yb^{3+} co-doped $BaMoO_4$ phosphors, J. Lumin. 210 (2019) 119–127. https://doi.org/10.1016/j.jlumin.2019.01.065.

[71]   W. Xu, X. Gao, L. Zheng, P. Wang, Z. Zhang, W. Cao, Optical Thermometry through Green Upconversion Emissions in Er^{3+}/Yb^{3+}-Codoped CaWO4 Phosphor, Appl. Phys. Express. 5 (2012) 072201. https://doi.org/10.1143/APEX.5.072201.

[72]   R. Lisiecki, M. Łukaszewicz, B. Klimesz, W. Ryba-Romanowski, Er^{3+},Yb^{3+}-doped oxyfluorotellurite glasses—Impact of temperature on spectroscopic properties and optical sensor qualities, J. Non. Cryst. Solids. 535 (2020) 119965. https://doi.org/10.1016/j.jnoncrysol.2020.119965.

[73]   A. Kumar, J. Manam, Optical thermometry using up and down conversion photoluminescence mechanism in Y2Zr2O7: Er^{3+} phosphors with excellent sensing sensitivity, J. Alloys Compd. 829 (2020) 154610. https://doi.org/10.1016/j.jallcom.2020.154610.

[74]   Z. Fang, L. Zhao, Q. Yang, Z. Yang, Y. Cai, D. Zhou, X. Yu, J. Qiu, X. Xu, Optical thermometry properties of silicate glass ceramics with dual-phase for spatial isolation of Er^{3+} and Cr^{3+}, J. Lumin. 219 (2020) 116861. https://doi.org/10.1016/j.jlumin.2019.116861.

[75]   A. Ćirić, J. Aleksić, T. Barudžija, Ž. Antić, V. Đorđević, M. Medić, J. Periša, I. Zeković, M. Mitrić, M.D. Dramićanin, Comparison of Three Ratiometric Temperature Readings from the Er^{3+} Upconversion Emission, Nanomaterials. 10 (2020) 627. https://doi.org/10.3390/nano10040627.

[76]   Y. Zhao, G. Bai, Y. Hua, Q. Yang, L. Chen, S. Xu, Optical thermometry based on upconversion emission of Yb^{3+}/Er^{3+} codoped bismuth titanate microcrystals, J. Lumin. 221 (2020) 117037. https://doi.org/10.1016/j.jlumin.2020.117037.

[77]   F. Huang, Y. Gao, J. Zhou, J. Xu, Y. Wang, Yb^{3+}/Er^{3+} co-doped $CaMoO_4$: A promising green upconversion phosphor for optical temperature sensing, J. Alloys Compd. 639 (2015) 325–329. https://doi.org/10.1016/j.jallcom.2015.02.228.

[78]   B. Dong, D.P. Liu, X.J. Wang, T. Yang, S.M. Miao, C.R. Li, Optical thermometry through infrared excited green upconversion emissions in Er^{3+}–Yb^{3+} codoped Al2O3, Appl. Phys. Lett. 90 (2007) 181117. https://doi.org/10.1063/1.2735955.

[79]   R.G. Geitenbeek, P.T. Prins, W. Albrecht, A. van Blaaderen, B.M. Weckhuysen, A. Meijerink, $NaYF_4$: Er^{3+}, Yb^{3+}/SiO_2 Core/Shell Upconverting Nanocrystals for Luminescence Thermometry up to 900 K, J. Phys. Chem. C. 121 (2017) 3503–3510. https://doi.org/10.1021/acs.jpcc.6b10279.

[80]   F. Hu, S. Lu, Y. Jiang, R. Wei, H. Guo, M. Yin, Optical thermometry based on upconversion luminescence behavior in $BaGdF_5$:Er^{3+} glass ceramics, J. Lumin. 220 (2020) 116971. https://doi.org/10.1016/j.jlumin.2019.116971.

[81]   S.F. León-Luis, V. Monteseguro, U.R. Rodríguez-Mendoza, M. Rathaiah, V. Venkatramu, A.D. Lozano-Gorrín, R. Valiente, A. Muñoz, V. Lavín, Optical nanothermometer based on the calibration of the Stokes and upconverted green emissions of Er^{3+} ions in $Y_3Ga_5O_{12}$ nano-garnets, RSC Adv. 4 (2014) 57691–57701. https://doi.org/10.1039/c4ra11565a.

CRediT authorship contribution statement

M.A. Hernández-Rodríguez: Conceptualization, Investigation, Formal analysis, Writing – original draft & Writing – review and editing.

K. Kamada & A. Yoshikawa: Resources

J.E. Muñoz-Santiuste: Resources, Methodology, Software & Formal analysis

A. Casasnovas-Melián: Formal analysis

I.R. Martín, U.R. Rodríguez-Mendoza & V. Lavín: Conceptualization, Supervision & Writing – review and editing.

Declaration of interests

☒ The authors declare that they have no known competing financial interests or personal relationships that could have appeared to influence the work reported in this paper.

☐The authors declare the following financial interests/personal relationships which may be considered as potential competing interests:

Highlights

- $Y_3Ga_5O_{12}:Er^{3+}$ garnet crystal got via micro-pulling down method for optical sensing.
- Remarkable temperature sensitivities and resolution from RT up, and beyond, 1000 K.
- Potential use as optical sensor for ultra-high temperature industrial applications.